AGU PUBLICATIONS

JGR

Journal of Geophysical Research: Space Physics

RESEARCH ARTICLE

10.1002/2013JA019672

Key Points:
- We model ULF waves and electron dynamics following an SSC
- Observations of 25 November 2001 SSC are reproduced by the model
- The SSC launches ULF waves which energize electrons by drift resonance

Correspondence to:
A. W. Degeling,
degeling@ualberta.ca

Citation:
Degeling, A. W., R. Rankin, and Q.-G. Zong (2014), Modeling radiation belt electron acceleration by ULF fast mode waves, launched by solar wind dynamic pressure fluctuations, *J. Geophys. Res. Space Physics*, *119*, 8916–8928, doi:10.1002/2013JA019672.

Received 3 DEC 2013
Accepted 28 SEP 2014
Accepted article online 4 OCT 2014
Published online 13 NOV 2014

Modeling radiation belt electron acceleration by ULF fast mode waves, launched by solar wind dynamic pressure fluctuations

A. W. Degeling[1]*, R. Rankin[1], and Q.-G. Zong[2]

[1]Department of Physics, University of Alberta, Edmonton, Alberta, Canada, [2]Institute of Space Physics and Applied Technology, Peking University, Beijing, China

Abstract We investigate the magnetospheric MHD and energetic electron response to a Storm Sudden Commencement (SSC) and subsequent magnetopause buffeting, focusing on an interval following an SSC event on 25 November 2001. We find that the electron flux signatures observed by LANL, Cluster, and GOES spacecraft during this event can largely be reproduced using an advective kinetic model for electron phase space density, using externally prescribed electromagnetic field inputs, (herein described as a "test-kinetic model") with electromagnetic field inputs provided by a 2-D linear ideal MHD model for ULF waves. In particular, we find modulations in electron flux phase shifted by 90° from the local azimuthal ULF wave electric field (E_ϕ) and a net enhancement in electron flux after 1.5 h for energies between 500 keV and 1.5 MeV near geosynchronous orbit. We also demonstrate that electrons in this energy range satisfy the drift resonance condition for the ULF waves produced by the MHD model. This confirms the conclusions reached by Tan et al. (2011), that the energization process in this case is dominated by drift-resonant interactions between electrons and MHD fast mode waves, produced by fluctuations in solar wind dynamic pressure.

1. Introduction

One of the outstanding problems in understanding the dynamic variations in the Earth's outer radiation belt has been the determination of observational signatures that can be attributed to a specific dynamical process. For example, it has been considered that the generation of growing localized peaks in electron phase space density with L shell must be evidence of a local acceleration process [*Green and Kivelson*, 2004; *Horne et al.*, 2005] (i.e., breaking the first adiabatic invariant), because diffusive radial transport [*Schulz and Lanzerotti*, 1974] (preserving the first invariant) cannot give rise to a growing localized peak. This has been shown not to be the case, however, if the radial transport is not diffusive [*Ukhorskiy et al.*, 2006a; *Degeling et al.*, 2008], as is the case when electrons are transported by drift resonance with narrow-band ULF waves [*Elkington et al.*, 1999].

On the other hand, the observational signatures suggesting drift resonance, such as coherent modulations of electron phase space density (PSD) over a range of energies, [*Claudepierre et al.*, 2013; *Mann et al.*, 2013; *Ukhorskiy et al.*, 2006b; *Degeling and Rankin*, 2008], also need to be interpreted carefully. For example, how can such modulations be distinguished from drift echoes [*Roederer*, 1970] (due to a particle injection unrelated to ULF wave activity), or from nonresonant particle motion in the presence of local ULF fluctuations? Moreover, does the paradigm of drift-resonant acceleration apply in highly dynamic situations, such as sudden storm commencement (SSC) events associated with the arrival of transient solar wind structures, such as shock fronts [*Elkington et al.*, 2013] and ULF fluctuations carried by the solar wind [*Kepko et al.*, 2002]?

In this paper we model the effect of magnetospheric MHD fast mode waves launched by dynamic pressure variations in the solar wind on the Earth's radiation belt electron population. We focus on an SSC event that occurred on 25 November 2001 [*Tan et al.*, 2011] and seek to identify the characteristics of the solar wind structure during this event that give rise to observed energetic electron flux signatures measured by LANL satellites. In particular, we investigate the effectiveness of the first and second solar wind pressure pulses during this event, compared to the subsequent ULF fluctuations, in launching ULF waves within the magnetosphere. This study is carried out using a 2-D linear ideal MHD model for ULF waves and an advective kinetic model for electron phase space density, using externally prescribed electromagnetic field inputs, (herein described as a "test kinetic model") for equatorially mirroring electrons [*Degeling et al.*, 2013].

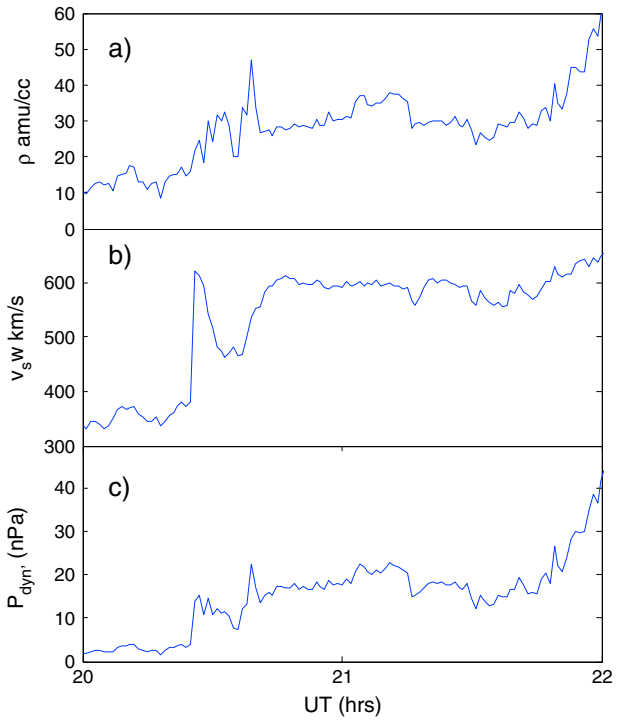

Figure 1. Geotail satellite solar wind observations during the interval from 20 to 22 UT on 25 November 2001: (a) mass density, (b) solar wind velocity, and (c) dynamic pressure. The satellite at this time is positioned at [*X*,*Y*,*Z*] (GSE) = [11.7,−17.1,−0.5] R_E, i.e., close to the magnetopause but still in interplanetary space.

2. Event Study: SSC on 25 November 2001

Before proceeding, it is necessary to give a short overview of the SSC event under examination, which occurred on 25 November 2001 and has been described in detail by *Tan et al.* [2011]. At approximately 2025 UT, the first of two pulses in dynamic pressure P_{Dyn}, marked the arrival of a solar wind shock front to the vicinity of Earth's magnetopause. These pulses were separated in time by about 15 min, the amplitude of each pulse was about 10 nPa (measured by the Geotail satellite, located at [*X*,*Y*,*Z*] (GSE) = [11.7,−17.1,−0.5] R_E, i.e., close to the magnetopause, but still in interplanetary space during the event). Figure 1 shows Geotail observations of solar wind plasma density and speed (Figures 1a and 1b, respectively) and calculated dynamic pressure (Figure 1c). These plots show that the first pulse in P_{dyn} is characterized by a transient jump in solar wind speed and an increase plasma density, while the second pulse is characterized by a transient jump in density and increase solar wind speed. The solar wind speed v_{sw} following the second pulse was measured to be 600 km/s. The bottom plot also shows ULF fluctuations in P_{dyn} following the first and second pulses.

The immediate geomagnetic effect of these disturbances in the solar wind are to abruptly compress the dayside magnetosphere and thereby launch a series of MHD fast mode waves within the magnetospheric cavity. This is evidenced by a sudden increase in equatorial magnetic field strength (60 nT at 6.6 R_E and 15 MLT measured by the GOES 8 satellite), sustained ULF wave electric field fluctuations of up to 15 mV/m measured by the Cluster 3 satellite (about 30° north of the equatorial plane near 12 MLT, crossing L = 6.6), and correlating ground-based ULF magnetic field fluctuations. By analyzing the phase delay in ground-based magnetometer signals at various MLT on the dayside, *Tan et al.* [2011] infers that the solar wind shock pulses initially impacted the magnetosphere in the early afternoon sector (about 14 MLT).

Fluctuations in electron flux that are phase correlated with ULF wave activity measured on Cluster 3 are observed for energies up to about 400 keV by the LANL 91 geosynchronous satellite (9–11 MLT), as well as the Cluster 3 satellite. An enhancement in energetic electron flux is also observed (for energies greater than 400 keV, measured by LANL 90, LANL 91, and GOES8 satellites), that appears to occur first on a time scale of a few minutes following the arrival of the SSC, and subsequently on a time scale of several minutes up to an hour. Unlike the lower energy electron flux, the flux at higher energies remains enhanced after some initial fluctuations, well after the ULF wave activity has decayed away. The fluctuations in electron flux at higher-energy channels do not appear well correlated with ULF wave phase. *Tan et al.* [2011] interprets the short time scale enhancement in energetic electron flux in terms of the sudden impulsive acceleration due to a sudden dayside magnetosphere compression, similar to the 24 March 1991 SSC event [*Blake et al.*, 1992; *Li et al.*, 1993]. However, the observations of high-energy electron flux over longer times scales are interpreted as evidence for drift-resonant electron energization by magnetospheric MHD fast mode waves. These ULF waves are interpreted by *Tan et al.* [2011] to be launched by solar wind dynamic pressure fluctuations following the SSC.

3. Model Overview

3.1. ULF Wave Model

We use the 2-D plus t finite element model for linear ideal MHD ULF waves in a box magnetic field geometry, described in *Degeling et al.* [2011], to calculate the wave-like perturbations to the electric and magnetic field arising from dynamic pressure fluctuations carried by the solar wind. A brief review is given here, emphasizing some modifications made to the model for the purposes of this paper. The interested reader is directed to *Degeling et al.* [2011] for more information.

Low-frequency waves satisfying ideal MHD can be modeled by the following linear equations:

$$\frac{\partial \mathbf{b}}{\partial t} = -\nabla \times \mathbf{E} \tag{1}$$

$$\frac{1}{v_A^2}\frac{\partial \mathbf{E}}{\partial t} = (\nabla \times \mathbf{b})_\perp - \frac{(\mu_o \mathbf{J} \times \mathbf{b}) \times \mathbf{B}_o}{B_o^2} + \mu_o \mathbf{J}^{ext} \tag{2}$$

where $\mathbf{B}_o$ is the unperturbed geomagnetic field, $\mu_o \mathbf{J} = \nabla \times B_o$ is the associated current density, $\mathbf{b}$ and $\mathbf{E}$ are the perturbed magnetic and electric fields, respectively, v_A is the Alfvén speed and $\mathbf{J}^{\text{ext}}$ is a perpendicular current source term for launching waves. The above equations are combined into a single hyperbolic PDE by taking the time derivative of equation (2) before being solved numerically; therefore, the source term for ULF waves appearing in the model has the form of $\partial \mathbf{J}^{\text{ext}}/\partial t$.

This model describes the propagation across the magnetic field of MHD fast mode waves, (identified by *Tan et al.* [2011] as poloidal mode waves with predominantly azimuthal electric field component [*Hughes and Southwood*, 1976]) launched by the wave source term $\partial \mathbf{J}^{\text{ext}}/\partial t$ and linear mode coupling to shear Alfvén waves on field lines where the fast mode wave frequency matches an eigenfrequency for standing waves. Such locations develop a characteristic peak and associated phase change in the equatorial electric field and are known as field line resonances (FLRs) [*Rankin et al.*, 2006; *Allan and Knox*, 1979; *Allan and Poulter*, 1992; *Samson et al.*, 1971].

In this investigation, we are interested in the process by which solar wind shock structures and pressure fluctuations couple to ULF waves in the magnetosphere by buffeting the magnetopause boundary.

We therefore define a parabolic surface representing an outer boundary on which the time-dependent source term for ULF waves $\partial \mathbf{J}^{\text{ext}}/\partial t$ is localized in our model and consider the arrival of planar wave fronts with a defined propagation velocity $\mathbf{v}_{\text{sw}}$ onto this surface. For example, if $\mathbf{R}_{\text{ext}}$ is a surface along which the ULF wave source term is localized, then the time delay for the arrival of a signal carried at $\mathbf{v}_{\text{sw}}$ is $\Delta t = \left((\mathbf{R}_{\text{ext}} - \mathbf{R}_o) \cdot \mathbf{v}_{\text{sw}}\right)/v_{\text{sw}}^2$, where $\mathbf{R}_o$ is the point of first contact for the solar wind wave fronts on the surface $\mathbf{R}_{\text{ext}}$.

Equation (2) when crossed with the magnetic field is the ideal MHD momentum conservation equation, in which the external current term $\mathbf{J}^{\text{ext}} \times \mathbf{B}_o$ represents the application of an external force. We associate this term with the force due to perturbations in the solar wind dynamic pressure gradient $\nabla P_{\text{dyn}}(t)$. Therefore, the ULF wave source term input to the model is set proportional to $\partial P_{\text{dyn}}/\partial t$ and is directed normal to the boundary surface.

Solar wind perturbations must first pass across the bow-shock and through the magnetosheath before reaching the magnetopause, which affects the coupling of solar wind perturbations to ULF waves within the magnetosphere [*Walker*, 1998]. This is included to a limited extent in our model by positioning the ULF wave source along the bow-shock boundary rather than the magnetopause, as used previously [*Degeling et al.*, 2013]. The bow shock boundary is modeled as a parabola with the same focus as the magnetopause boundary, with a 5 R_E distance separating the two surfaces along the noon meridian.

The magnetosheath plasma is modeled simplistically by a constant mass density. The mass density within the magnetosphere is specified using the analytic model of *Denton et al.* [2004], and the transition between magnetosheath and magnetosphere density is modeled using a smooth transition function across the magnetopause boundary (of the form $0.5\left(1 - \sin\left(\pi\left(x - x_o\right)/2\Delta x\right)\right)$, where x is the perpendicular distance across the boundary located at x_o and Δx is the boundary thickness).

3.2. Equatorially Mirroring Electrons

We take a similar approach to *Degeling et al.* [2011] and consider the dynamics of equatorially mirroring electrons, for which the guiding center equation of motion is [*Northrop*, 1963]

$$\mathbf{v} = \frac{\mathbf{E}\times\mathbf{B}}{B^2} + \frac{M}{q\gamma}\frac{\mathbf{B}\times\nabla\mathbf{B}}{B^2} \tag{3}$$

where $\gamma = \left(1 + 2MB/m_e c^2\right)^{1/2}$ is the relativistic correction factor and first adiabatic invariant M, charge q, mass m_e, and speed of light c are constants.

The above equation is used to drive a test kinetic simulation for phase space density (PSD) $f = f(r, \phi, M, t)$ within the magnetosphere. This is done by assuming an initial distribution of the form $f = f_i\left(L_o, M\right)$ and solving the advection equation for PSD:

$$\frac{\partial f}{\partial t} + \mathbf{v}\cdot\nabla f = 0 \tag{4}$$

This equation is solved numerically on a fixed polar coordinate grid using operator splitting and a 1-D flux corrected transport algorithm, with equation (3) calculated using fields interpolated from the ULF wave model. The initial PSD is given by a Kappa distribution [*Livadiotis and McComas*, 2013], as a function of kinetic energy $W = m_e c^2\left(\gamma - 1\right)$, given by

$$f_i(W) = f_o\left(1 + \frac{W}{\kappa W_{th}}\right)^{-(\kappa+1)} \tag{5}$$

where the following constant values are set: $f_o = 1$, $\kappa = 4$, and the effective thermal energy $W_{\mathrm{th}} = 10$ keV. This functional form implies that the initial PSD at constant M monotonically increases with L (due to the L dependence of the magnetic field strength), which is expected for diffusion-dominated radial transport in the absence of internal sinks or sources of electrons. As shown in section 4.2, Figures 5 and 6, these values give an initial electron flux distribution that scales with energy in a similar manner to the LANL observations prior to SSC reported in *Tan et al.* [2011].

We include particle loss through the magnetopause (magnetopause shadowing [*West et al.*, 1972; *Shprits et al.*, 2006; *Turner et al.*, 2012, 2013]) by simply adding the rule for each time step in the calculation that $f_o\left(L_o, M\right) = 0$ for points outside the magnetopause boundary. We account for motion of the magnetopause boundary by integrating the ideal MHD velocity equation $\mathbf{v} = \left(\mathbf{E}\times\mathbf{B}\right)/B^2$ in order to evaluate the displacement of points along the magnetopause. This motion is included in the above consideration of particle losses through the magnetopause. Since the electron transport model deals with guiding center motion only, the effect of finite Larmor radius on magnetopause shadowing for higher-energy electrons is not included. Therefore, losses to the magnetopause for higher-energy electrons may be underestimated in this study; however, this is unlikely to strongly impact the results presented.

4. Results

4.1. Driving the ULF Wave Model Using Solar Wind Dynamic Pressure Fluctuations

Figure 2 shows a series of frames of the magnetosphere equatorial plane, as the modeled shock front and subsequent ULF fluctuations (derived from the time series shown in Figure 1) impact the magnetosphere obliquely in the early afternoon sector (first contact at 14 MLT). This figure demonstrates significant ULF wave activity, particularly following the first and second pulses in dynamic pressure (arriving at 2027 UT and 2038 UT). These frames show the antisunward propagation of MHD fast mode waves (in E_ϕ) with reasonably low azimuthal wave numbers m (i.e., $m < 10$) along the flanks and a radial standing wave structure on the dayside magnetosphere in the afternoon sector. The restriction in m is due to the fact that the MHD fast mode turning point generally occurs at higher L shell as m is increased [*Allan and Poulter*, 1992]. For this reason the excitation of high m ULF waves by an external magnetopause driver is extremely difficult, even in the case of a compressed magnetosphere, where the breakage in azimuthal symmetry (compared to a dipole, for example) gives rise to coupling between azimuthal modes [*Degeling et al.*, 2011]. A notable exception would be the case where a highly MLT-structured plasmaspheric drainage plume exists in the afternoon sector, because in this case the corresponding Alfvén speed structure would introduce coupling between waves with widely differing azimuthal mode numbers. This is a topic that will be explored in future work.

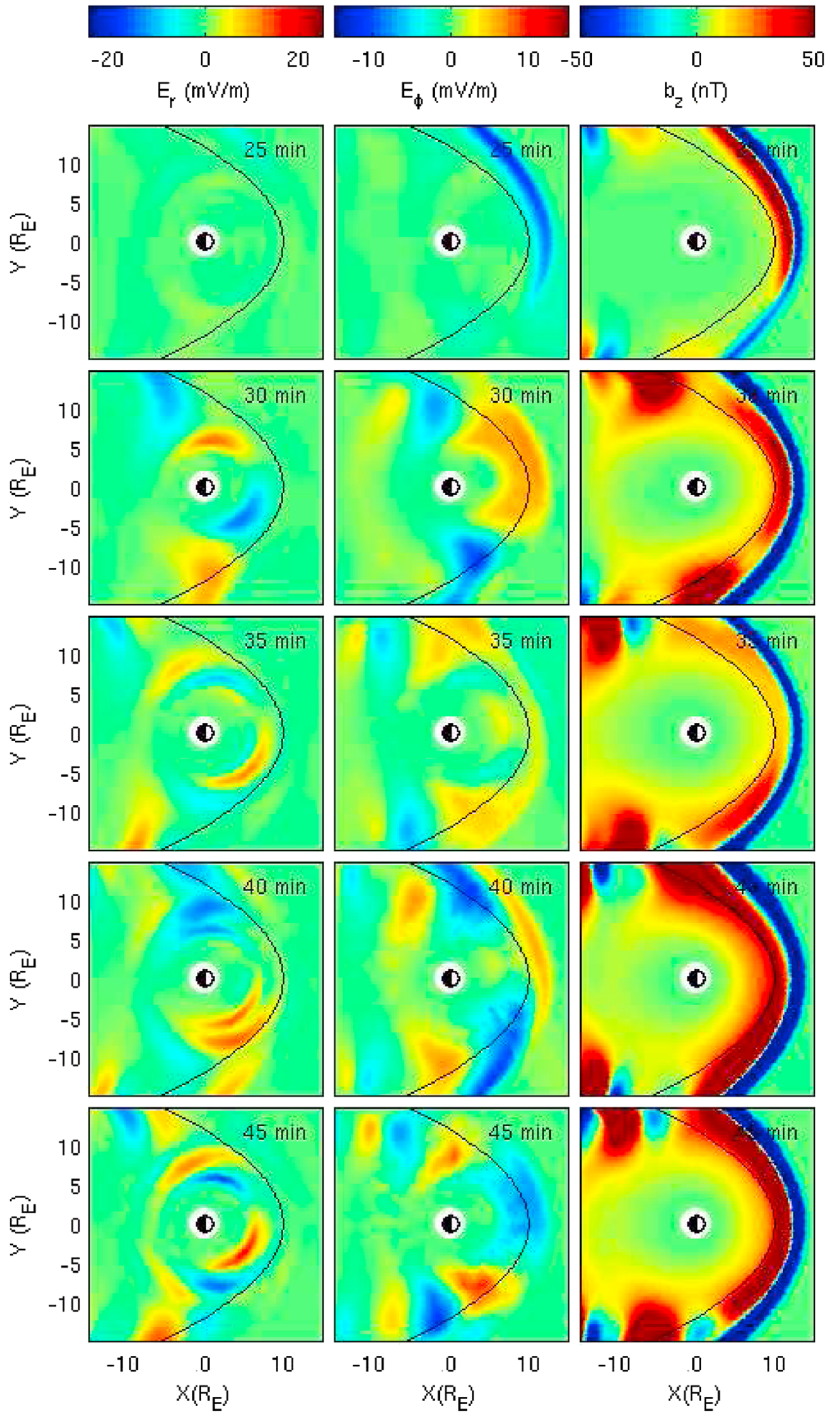

Figure 2. The ULF wave model outputs driven by Geotail dynamic pressure time series shown in Figure 1, showing: (left) E_r (mV/m), (center) E_ϕ (mV/m), and (right) b_z (nT). Time in minutes after 20 h UT is indicated.

The radial electric field (E_r) exhibits fine radial structure due to the phase mixing of multiple field line resonances (with low m) across a range of L shells from 5 to 8 R_E. The positive bias of the $\partial P_{dyn}/\partial t$ driving signal gives rise to a net increase in the perturbed magnetic field b_z, indicating compression of the dayside magnetosphere. Figure 3 shows time series of E_r, E_ϕ, and b_z and their corresponding spectral power density (for E_r and E_ϕ), at $L = 4.4$ and 6.6, for 9 and 15 h MLT. These figures show that the spectral power is significantly dependent on L shell. The peak frequency of the E_r component increases strongly with decreasing L shell because of the resonant coupling of MHD fast wave power to shear Alfvén modes (with small

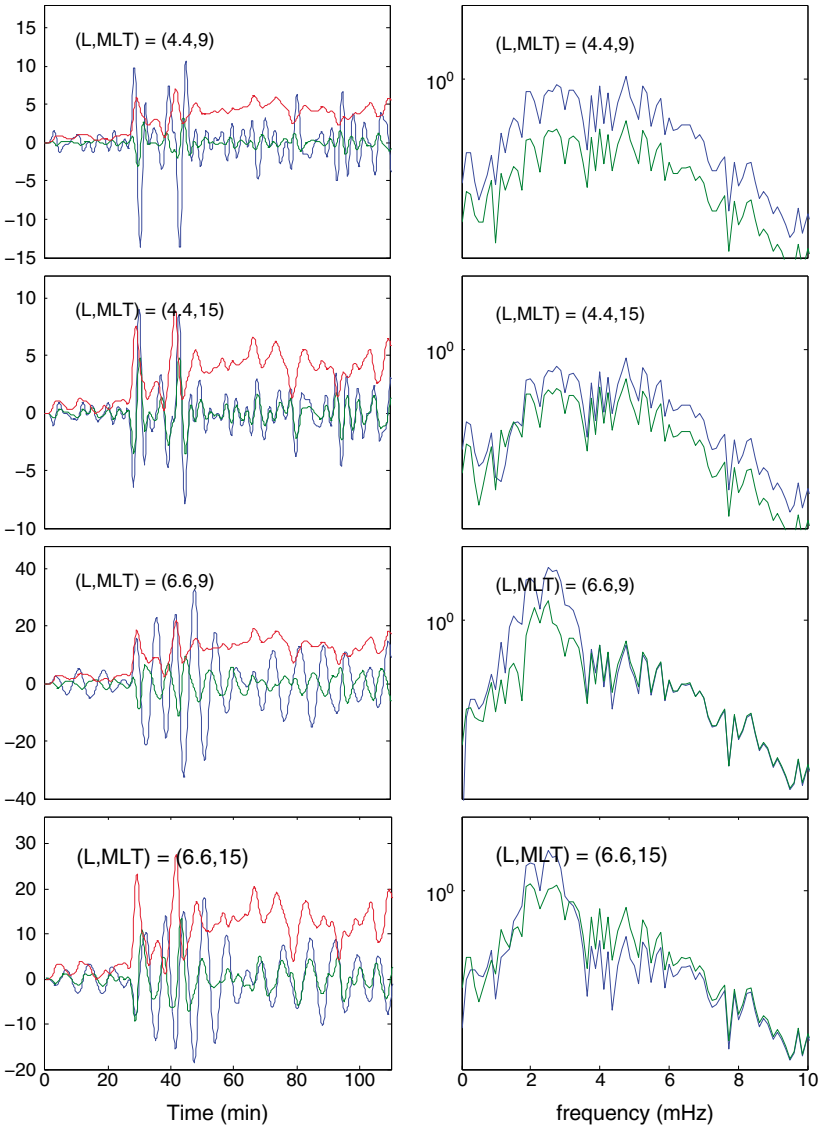

Figure 3. (left column) Time series for the ULF wave fields E_r (mV/m), E_ϕ (mV/m), and b_z (nT) (blue, green, and red, respectively). (right column) Power spectral densities for E_r and E_ϕ $(\mathrm{mV/m})^2/\mathrm{mHz}$ (blue and green, respectively).

azimuthal mode number m), which have higher frequency fundamental modes as L shell is decreased while outside the plasmasphere. In the case of MHD fast mode waves, the location of the turning point for these waves within the magnetosphere varies with the wave frequency [*Allan and Poulter*, 1992], such that lower frequency waves are cut off with decreasing L shell, leaving power at higher frequencies.

Ground-based observations using pairs of longitudinally spaced magnetometers were used by *Tan et al.* [2011] to estimate a local azimuthal mode number m during the SSC event. Two values were reported based on the relative phase delay between the pairs of magnetometers: $m = -3$ close to 12 MLT, and $m = +1$ at 23 MLT. In order to compare our ULF wave model results against these observations, we estimate the local azimuthal mode number by analyzing the phase of the ULF wave electric field, using the following algorithm. First, we take the component (E_d) of **E** parallel to the contours of constant B (since this component is the most relevant for drift resonance wave-particle interactions, discussed in the next section). We then model this component as $E_d(r,\phi,t) = |E_d| \exp(i\Psi)$, by taking the Hilbert transform of E_d in time. The phase $\Psi(r,\phi,t)$ is found by taking the angle argument of the complex signal. The local wave vector **k** can therefore be estimated by $\nabla\Psi$, and the local wave frequency can be estimated by $-\partial\Psi/\partial t$. Lastly, the local azimuthal mode number is given by $m = \nabla\Psi \cdot \mathbf{e}_\phi$. Equatorial maps of Ψ and m evaluated as described above are shown

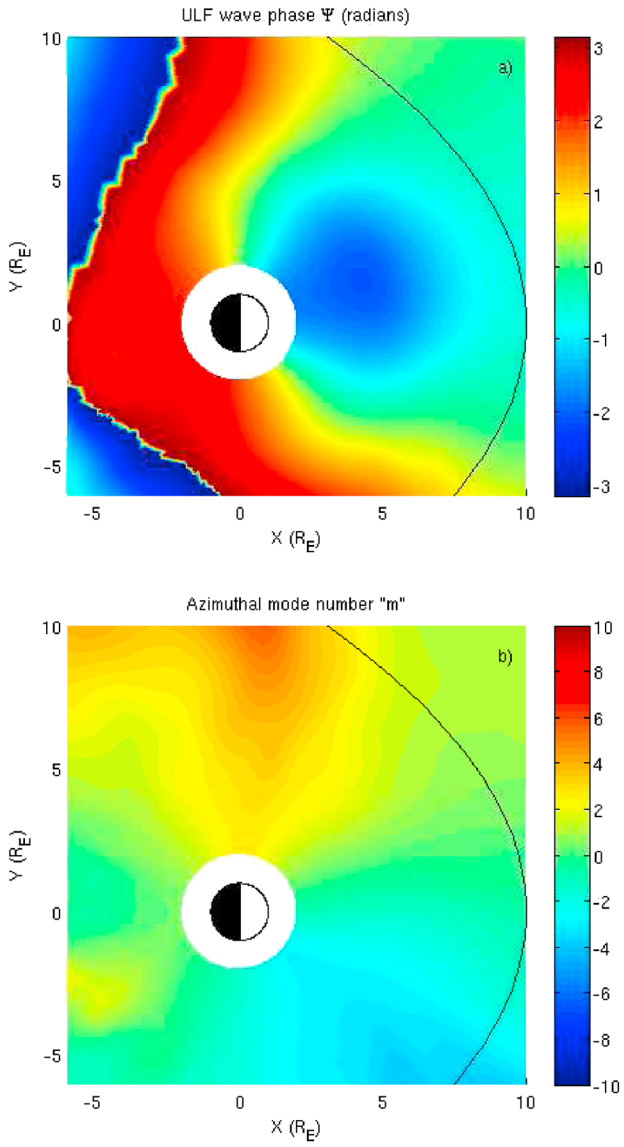

Figure 4. (a) Equatorial map taken at 2032 UT, showing the angular phase of the electric field component parallel to the electron drift direction. (b) The azimuthal mode number "m" calculated from the phase data shown in Figure 4a.

in Figures 4a and 4b, respectively, taken approximately 5 min after the initiation of the SSC. These figures show that $m \approx 0$ in the post noon and post midnight sectors, corresponding to an axis that is roughly in the direction of incidence of the solar wind dynamic pressure pulses. The maximum and minimum local m values are $\pm$(5–10), occurring around 18 MLT and 10 MLT, respectively. The results shown in the figure roughly correspond with the observed values of −3 around 12 MLT, and +1 around 23 MLT, and indicate that the low m value near local midnight is because the ULF waves are propagating tailward in this sector. These model results confirm the inference made by *Tan et al.* [2011], based on observations of $m = -3$ waves propagating across the noon sector, that ULF waves are also propagating down the magnetosphere flank in the afternoon sector and have positive m values of similar magnitude (i.e., corresponding to propagation in the direction of the electron drift), allowing the possibility of drift resonance interactions.

4.2. Electron Response: Comparison With Observations

The test kinetic model was run using the ULF wave model electric and magnetic field data as inputs, for a range of M values logarithmically spaced between 0.1 and 20 keV/nT. In order to directly compare with LANL satellite observations, the phase space density $f(M, L, \phi, t)$ output from the model was converted to electron flux $J = 2m_e MBf$, where $B(L, \phi, t)$ is the local equatorial magnetic field strength. The electron flux was then remapped to a function of kinetic energy $J = J(W, L, \phi, t)$ where $W = m_e c^2(\gamma - 1)$, and the result averaged over a set of nine energy bins between 50 keV and 1.5 MeV, similar to the energy channels used on LANL spacecraft.

Figure 5 shows the electron flux for the case driven by ULF waves shown in Figure 2, interpolated to the approximate location of the LANL91 satellite (L = 6, MLT = 11) during the event. Figure 5 (top) shows the E_ϕ signal interpolated at the same location. The binned electron flux in the lower panel shows an initial enhancement, corresponding to the passage of the dynamic pressure pulse, followed by a series of modulations that appear to be synchronized with positive zero crossing in E_ϕ for the first half hour following the SSC. The electron flux across all energy levels increases above their pre-SSC values in the first 20 min (peaking soon after the arrival of the second P_{dyn} pulse); however, the lower energy channels (W<150 keV) return to roughly the same values after 90 min. On the other hand, the higher-energy channels each show an average increase in flux over the pre-SSC levels, by a factor of between 2 and 5. Figure 6 shows a similar plot for binned electron flux interpolated to the approximate location of the LANL90 satellite during

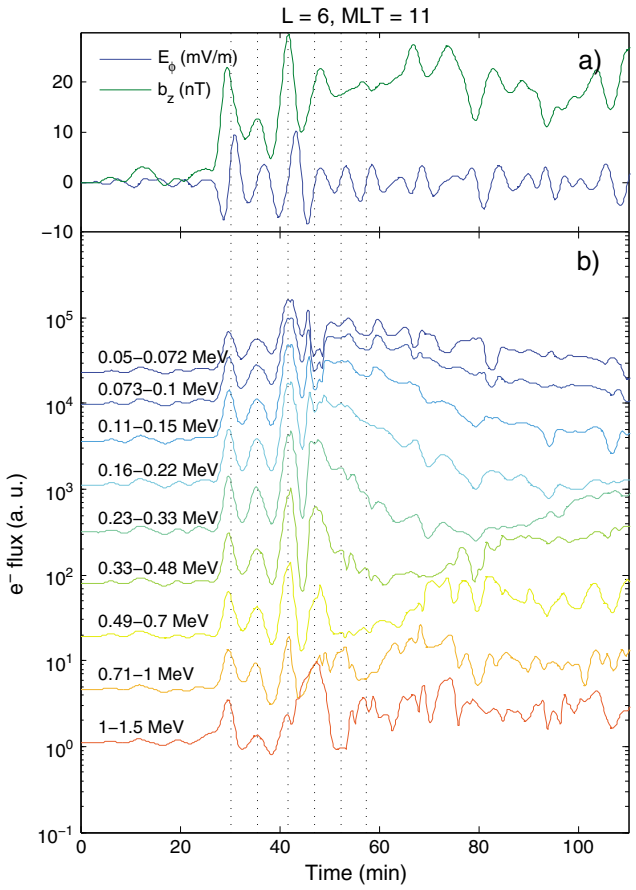

Figure 5. Test kinetic model electron flux output interpolated at $L = 6$, 11 MLT (LANL91) (top) E_ϕ and (bottom) b_z time series. Electron flux time series for energy bins indicated. Vertical-dotted lines mark the positive zero crossings in E_ϕ. Time is measured from 20 h UT.

the event ($L = 6$, MLT = 17 h) and shows similar behavior in the electron flux time series. These results are qualitatively similar to the observations reported in *Tan et al.* [2011, Figures 9 and 10].

These electron flux results are necessarily dependent on the choice of the initial PSD f_i in the model, given by equation (5). The LANL observations prior to SSC were used to constrain κ and W_{th} in this equation; however, it is not clear how the initial PSD should scale with L, keeping W constant (since LANL observations correspond to a single L). It can be shown that the AE-8 trapped electron model *Vette* [1991] is broadly consistent with equation (5), with $f_o \propto L_o^{-\nu}$ (where ν is a positive constant); therefore, we make this change to equation (5). Scanning values of ν, we found qualitatively similar results to those presented in Figures 5 and 6 for $\nu < 2$; however, we found that fluctuations in electron flux in the lowest energy channels became significantly diminished as ν was further increased. This is due to a reduction in the L scaling of PSD holding M constant, introduced by the $L_o^{-\nu}$ acting in opposition to L scaling in PSD due to the magnetic field. As this trend is not consistent with the observations, we maintain a value of $\nu = 0$ (i.e., constant f_o) for the initial PSD.

One systematic difference between our model results and the observations of *Tan et al.* [2011] is that we found the electron flux behavior at a lower L shell more closely corresponded with the LANL observations (i.e., $L = 6.0$ instead of $L = 6.6$). We found that the electron flux became considerably depleted for $L > 6.3$ in our model, due to magnetopause shadowing during the initial compression of the dayside magnetosphere. The most likely source of this discrepancy is that our model of magnetopause motion leads to an overestimation of the dayside compression due to the solar wind pressure pulses. In this case we expect that the electron flux depletions predicted by the model for $L > 6.3$ may be occurring at higher L shells in the actual event. There is some evidence of magnetopause shadowing in the LANL91 data shown in Figure 10 of *Tan et al.* [2011]. This figure shows a number of sharp, momentary depletions of up to a factor of 10 in flux, for channels up to about 300 keV in energy, occurring between 2100 UT and 2145 UT. This is unlikely to be the result of the spacecraft crossing the magnetopause boundary, because the flux depletions signifying such a crossing would occur across all energy channels.

The magnetopause shadowing effect is illustrated in Figure 7, which shows contour plots of the ratio $J(W, L, t)/J(W, L, t = 0)$ for four different energy bins, for a meridian slice along 11 MLT. The loss (by greater than a factor of 10 compared to pre-SSC values) for each energy bin due to magnetopause shadowing is visible for upper L shells in each plot, with a clearly marked interface in L that fluctuates with time. A solid green line in each figure marks the time-dependent location of the magnetopause in these plots, which oscillates in time after the initial SSC pulse, in response to the ULF perturbations in solar wind dynamic pressure. These plots show that, for the higher energy ranges, the electron flux levels at high L shell are gradually repopulated by outward radial transport from lower L shells, over the 2 h interval displayed and that this refilling toward the magnetopause is more rapid at higher energies. Presumably, this outward transport

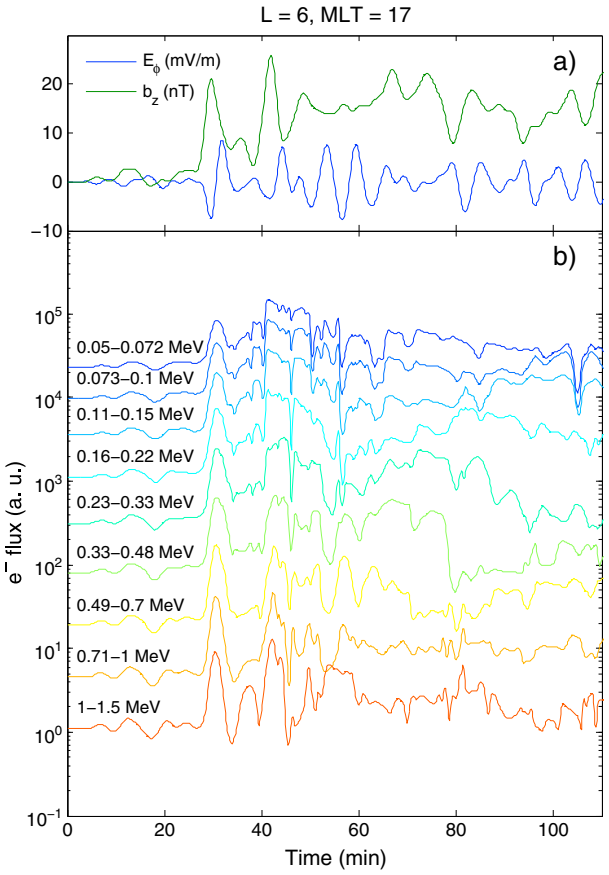

Figure 6. Test kinetic model electron flux output interpolated at $L = 6$, 17 h MLT (LANL90) (top) E_ϕ and (bottom) b_z time series. Electron flux time series for energy bins indicated. Time is measured from 20 h UT.

would continue to the magnetopause in the presence of continued ULF wave activity. This appears to be consistent with the observed energy dependence of magnetopause shadowing loss reported over longer timescales in other event studies [*Bortnik et al.*, 2006].

Figure 7 also shows that the qualitative behavior described earlier for Figure 5, namely, a transient enhancement for lower energies and a more sustained enhancement for higher energies, spans a range of L values from 5 to 7, depending on the energy bin.

The correspondence between our model results and the observations of the 25 November SSC event are suggestive of the interpretation put forward by *Tan et al.* [2011], that the observed enhancements in flux result from drift-resonant interactions between ULF MHD fast mode waves launched by solar wind fluctuations associated with the SSC. However, it could also be the case that the observed modulations in flux are due to the local advection of gradients in electron phase space density as the ULF waves pass by. If this is the case, then one would expect that any electron energization, or change in electron flux at a given energy, would be the result of local changes in the magnetic field strength only. Since we know the initial distribution of electrons in our model, we can simply check whether the flux changes shown in Figures 7 and 5 are consistent with this null hypothesis.

Assuming constant magnetic moment, it is simple to show that relative changes in magnetic field and kinetic energy are related by $\Delta W/W = 1/2\,(1 + 1/\gamma)\,\Delta B/B$. From the definition of the Kappa distribution (equation (5)), it can be shown that an estimate of the relative change in electron PSD $\Delta f/f$ due to the magnetic field change $\Delta B/B$ is given by

$$\frac{\Delta f}{f} = -\frac{(\kappa+1)}{2}\left(\frac{W/\kappa W_{th}}{1+W/\kappa W_{th}}\right)\left(\frac{W+2m_ec^2}{W+m_ec^2}\right)\frac{\Delta B}{B} \tag{6}$$

For example, considering 1 MeV electrons and $\kappa = 4$, this gives $\Delta f/f \approx -3\Delta B/B$. At $L = 6$ near local noon, $B = 180$ nT, and $\Delta B < 30$ nT (according to Figure 5); therefore, we would expect $\Delta f/f$ to be less than 50%. Figure 5 shows relative changes in electron flux by a factor of between 2 and 5 in the highest two energy channels (note that the relative change in electron flux in a constant energy channel is equivalent to $\Delta f/f$). This indicates that electrons contributing to these enhancements in energetic flux are being transported from regions where the magnetic field is significantly weaker, which is not consistent with localized back-and-forth advection that would be expected from nonresonant interactions as the ULF waves pass by.

We now examine the drift resonance hypothesis by considering whether drifting electrons can remain in phase with the propagating ULF waves for a significant portion of their orbit. In the scenario under consideration, where ULF waves originating from the magnetopause propagate antisunward, this can only happen in the afternoon/evening sector, since the electron drift direction and wave propagation are aligned in this

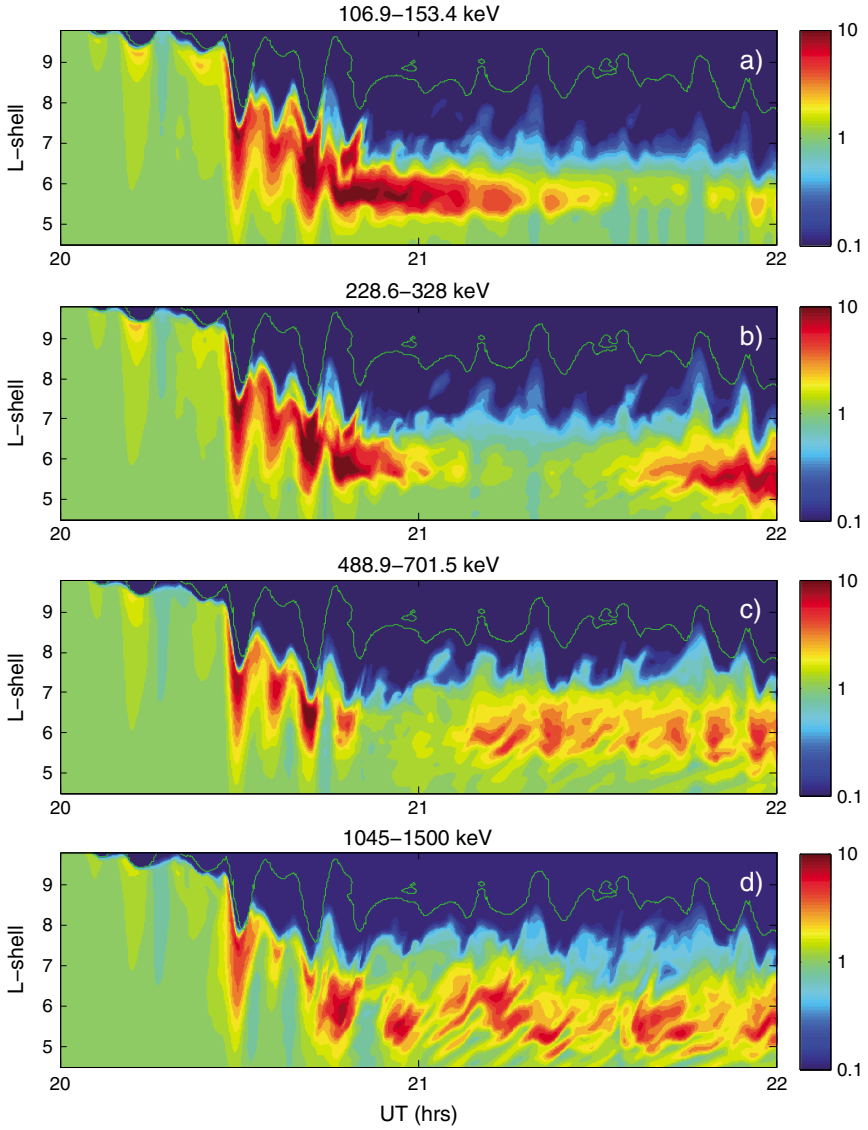

Figure 7. Contour maps showing the ratio $J(W, L, t)/J(W, L, t_o)$ (where t_o = 20 h UT) as a function of L shell and time, interpolated along the 11 MLT meridian, with binning in energy over the ranges indicated. The solid green line marks the time-dependent position of the magnetopause at this meridian.

region. In the following we consider the range of electron energies that are resonant with the waves in this region, and whether this corresponds with the range of energies and L shells in the model and observations where enhancements in electron flux are seen. Given the zeroth-order guiding center drift velocity for electrons (the second term in equation (3)) and estimates of the local ULF wave vector $\mathbf{k} = \nabla\Psi$, and frequency $\omega = -\partial\Psi/\partial t$ obtained from the ULF wave model in the previous section, the condition for local drift resonance $\mathbf{k} \cdot \mathbf{v}_d - \omega = 0$ may be expressed as follows:

$$\frac{M}{q\gamma B^2}(\nabla B \times \mathbf{B}) \cdot \nabla\Psi + \frac{\partial\Psi}{\partial t} = 0 \tag{7}$$

This may be rearranged as $\gamma^2 + P\gamma - 1 = 0$, where $P = (\partial\Psi/\partial t) / \left(\left(m_e c^2/2qB^3\right)\left(\nabla B \times \mathbf{B} \cdot \nabla\Psi\right)\right)$. Solving this equation for γ, we are able to obtain an estimate of the kinetic energy for electrons satisfying the resonant condition $W_{res} = m_e c^2\left(\gamma_{\text{res}} - 1\right)$. We restrict our attention to the region where the ULF wave electric field component in the direction of the electron drift has an amplitude greater than 2 mV/m. The result, plotted as a 2-D map in the equatorial plane for the same time slice as shown in Figure 4 is shown in Figure 8.

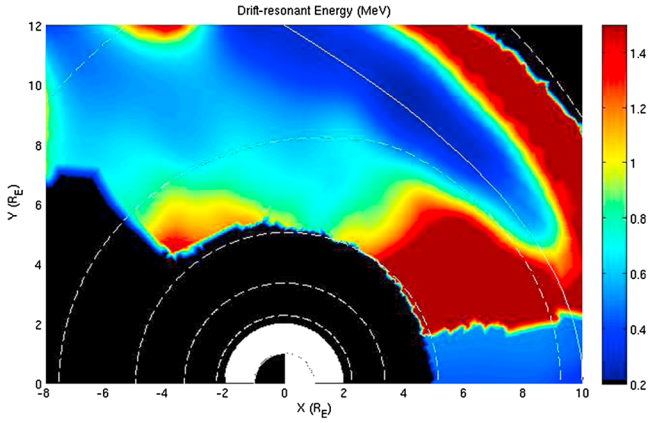

Figure 8. Equatorial map taken at 2032 UT, showing the electron energy that satisfies the drift resonance condition (equation (7)). Only areas where the amplitude of the electric field component parallel to the drift is greater than 2 mV/m are shown. Zeroth-order drift trajectories are shown as white dashed lines, and the nominal magnetopause location is shown by a white solid line.

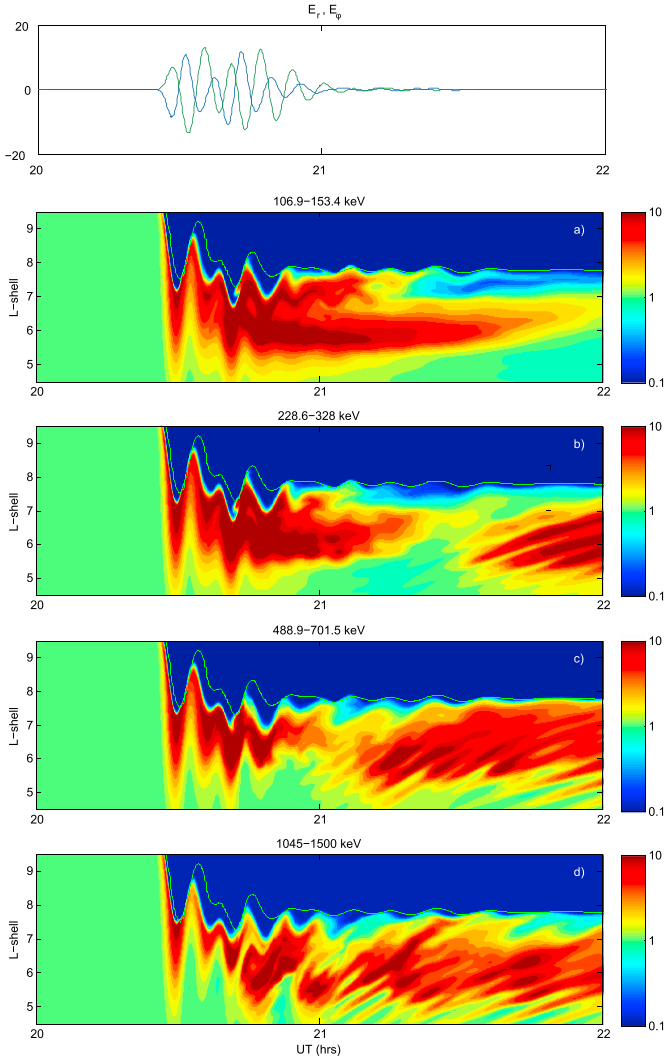

Figure 9. (top) Wave packets for E_r and E_ϕ at $L = 6$, 12 MLT resulting from the application of two isolated P_{dyn} pulses (each of amplitude 10 nPa) at 20.25 and 20.40 UT. (bottom four panels) Contour maps showing the ratio $J(W, L, t)/J(W, L, t_o)$ similar to Figure 7 for this case, interpolated along the 12 MLT meridian. The solid green line marks the time-dependent position of the magnetopause at this meridian.

This figure shows that electrons with energies in the range between 500 keV and 1.5 MeV are locally drift resonant with the ULF waves propagating in the afternoon sector between 15 MLT and 18 MLT, on drift orbits corresponding to L values from 5 to 7.

4.3. The Role of Solar Wind ULF Fluctuations Following the Shock

One of the interpretations put forward by *Tan et al.* [2011], was that the ULF wave fluctuations carried by the solar wind following the SSC launched MHD fast mode waves within the magnetosphere, by magnetopause buffeting, and that these waves were important for electron energization during a 2 h interval following the SSC. We test this by means of an idealized solar wind $P_{dyn}(t)$ signal, which consists of two discrete jumps of 10 nPa each, separated by a 15 min interval and no other ULF activity carried by the solar wind. All other ULF wave model parameters are left unchanged from the case studied earlier. This input signal drives an interval of ULF wave activity similar to that shown in Figure 2, although the duration of wave activity is less than an hour, as illustrated by Figure 9 (top). The bottom panels in Figure 9 show the change in electron flux as a function of L shell and time along the noon meridian for the same energy channels used in Figure 7 and shows a similar pattern of enhancement to that figure. This result indicates that ULF waves launched by the two initial dynamic pressure pulses dominate the electron energization process. It is important to point out that this process is not simply the inductive electric field due to the rapid compression of the dayside magnetopause. The action of this compression (or, the manner by which this compression takes place) launches MHD fast mode waves, which appear to be phase coherent for a sufficiently long time to resonantly interact with the electrons.

5. Conclusion

We have investigated the magnetospheric MHD and energetic electron response to the arrival of an SSC and subsequent magnetopause buffeting, focusing on a 1.5 h interval following an SSC on 25 November, 2001. We find that the electron flux signatures observed by LANL, Cluster, and GOES spacecraft during this event can be largely reproduced using a test kinetic electron dynamics simulation that ingests electromagnetic fields from a 2-D linear ideal MHD model for ULF waves. In particular, we see modulations in electron flux phase shifted by 90° from local E_ϕ, and a net enhancement after 1.5 h for energies from 300 keV up to 1.5 MeV. This confirms the conclusion reached by *Tan et al.* [2011], that the energization process in this case is dominated by drift-resonant interactions between electrons and MHD fast mode waves. We examine the notion that the ULF wave fluctuations carried by the solar wind provide a significant contribution to the energization process by testing the case where they are removed. We find similar levels of enhancement due to ULF waves launched by the solar wind dynamic pressure pulses only and, therefore, conclude that direct coupling of ULF wave power from the solar wind to waves in the magnetosphere does not provide a strong contribution to electron energization in this case.

Acknowledgments

The authors would like to thank Ian Mann, Louis Ozeke, Clare Watt, and Jonathan Rae for many insightful discussions. We also thank Mark Gordan and Andy Kale for computing infrastructure support. This work is partially supported by the Canadian Space Agency and Natural Sciences and Engineering Research Council of Canada.

Michael Balikhin thanks the reviewers for their assistance in evaluating this paper.

References

Allan, W., and F. Knox (1979), Effect of finite ionosphere conductivities on axisymmetric toroidal Alfven wave resonances, *Planet. Space Sci.*, *27*(7), 939–950.

Allan, W., and F. Poulter (1992), ULF waves—Their relationship to the structure of the Earth's magnetosphere, *Rep. Prog. Phys.*, *55*, 533–598.

Blake, J. B., W. A. Kolasinski, R. W. Fillius, and E. G. Mullen (1992), Injection of electrons and protons with energies of tens of MeV into L < 3 on 24 March 1991, *Geophys. Res. Lett.*, *19*(8), 821–824, doi:10.1029/92GL00624.

Bortnik, J., R. M. Thorne, T. O. O'Brien, J. C. Green, R. J. Strangeway, Y. Y. Shprits, and D. N. Baker (2006), Observation of two distinct, rapid loss mechanisms during the 20 November 2003 radiation belt dropout event, *J. Geophys. Res.*, *111*, A12216, doi:10.1029/2006JA011802.

Claudepierre, S. G., et al. (2013), Van Allen Probes observation of localized drift resonance between poloidal mode ultra-low frequency waves and 60 keV electrons, *Geophys. Res. Lett.*, *40*, 4491–4497, doi:10.1002/grl.50901.

Degeling, A. W., and R. Rankin (2008), Resonant drift echoes in electron phase space density produced by dayside Pc5 waves following a geomagnetic storm, *J. Geophys. Res.*, *113*, A10220, doi:10.1029/2008JA013254.

Degeling, A. W., L. G. Ozeke, R. Rankin, I. R. Mann, and K. Kabin (2008), Drift resonant generation of peaked relativistic electron distributions by Pc5 ULF waves, *J. Geophys. Res.*, *113*, A02208, doi:10.1029/2007JA012411.

Degeling, A. W., R. Rankin, and S. R. Elkington (2011), Convective and diffusive ULF wave driven radiation belt electron transport, *J. Geophys. Res.*, *116*, A12217, doi:10.1029/2011JA016896.

Degeling, A. W., R. Rankin, K. Murphy, and I. J. Rae (2013), Magnetospheric convection and magnetopause shadowing effects in ulf wave-driven energetic electron transport, *J. Geophys. Res. Space Physics*, *118*, 2919–2927, doi:10.1002/jgra.50219.

Denton, R. E., J. D. Menietti, J. Goldstein, S. L. Young, and R. R. Anderson (2004), Electron density in the magnetosphere, *J. Geophys. Res.*, *109*, A09215, doi:10.1029/2003JA010245.

Elkington, S., M. Hudson, and A. Chan (1999), Acceleration of relativistic electrons via drift-resonant interaction with toroidal-mode Pc5 ULF oscillations, *Geophys. Res. Lett.*, *26*(21), 3273–3276.

Elkington, S. R., A. A. Chan, and M. Wiltberger (2013), Global structure of ULF waves during the 24–26 September 1998 geomagnetic storm, in *Dynamics of the Earth's Radiation Belts and Inner Magnetosphere*, edited by D. Summers et al., pp. 127–138, AGU, Washington, D. C., doi:10.1029/2012GM001348.

Green, J. C., and M. G. Kivelson (2004), Relativistic electrons in the outer radiation belt: Differentiating between acceleration mechanisms, *J. Geophys. Res.*, *109*, A03213, doi:10.1029/2003JA010153.

Horne, R. B., et al. (2005), Wave acceleration of electrons in the Van Allen radiation belts, *Nature*, *437*(7056), 227–230, doi:10.1038/nature03939.

Hughes, W. J., and D. J. Southwood (1976), Screening of micropulsation signals by atmosphere and ionosphere, *J. Geophys. Res.*, *81*, 3234–3240, doi:10.1029/JA081i019p03234.

Kepko, L., H. E. Spence, and H. J. Singer (2002), Ulf waves in the solar wind as direct drivers of magnetospheric pulsations, *Geophys. Res. Lett.*, *29*(8), 39-1–39-4, doi:10.1029/2001GL014405.

Li, X., I. Roth, M. Temerin, J. R. Wygant, M. K. Hudson, and J. B. Blake (1993), Simulation of the prompt energization and transport of radiation belt particles during the March 24, 1991 SSC, *Geophys. Res. Lett.*, *20*(22), 2423–2426, doi:10.1029/93GL02701.

Livadiotis, G., and D. J. McComas (2013), Understanding kappa distributions: A toolbox for space science and astrophysics, *Space Sci. Rev.*, *175*, 183–214, doi:10.1007/s11214-013-9982-9.

Mann, I. R., et al. (2013), Discovery of the action of a geophysical synchrotron in the Earth'S Van Allen radiation belts, *Nat. Commun.*, *4*, 2795, doi:10.1038/ncomms3795.

Northrop, T. G. (1963), *The Adiabatic Motion of Charged Particles*, Interscience, New York.

Rankin, R., K. Kabin, and R. Marchand (2006), Alfvenic field line resonances in arbitrary magnetic field topology, *Adv. Space Res.*, *38*(8), 1720–1729, doi:10.1016/j.asr.2005.09.034.

Roederer, J. G. (1970), *Dynamics of Geomagnetically Trapped Radiation*, Springer, New York.

Samson, J. C., J. A. Jacobs, and G. Rostoker (1971), Latitude-dependent characteristics of long-period geomagnetic micropulsations, *J. Geophys. Res.*, *76*, 3675–3683.

Schulz, M., and L. J. Lanzerotti (1974), *Particle Diffusion in the Radiation Belts*, Springer, New York.

Shprits, Y. Y., R. M. Thorne, R. Friedel, G. D. Reeves, J. Fennell, D. N. Baker, and S. G. Kanekal (2006), Outward radial diffusion driven by losses at magnetopause, *J. Geophys. Res.*, *111*, A11214, doi:10.1029/2006JA011657.

Tan, L. C., X. Shao, A. S. Sharma, and S. F. Fung (2011), Relativistic electron acceleration by compressional mode ULF waves: Evidence from correlated Cluster, Los Alamos National Laboratory spacecraft, and ground based magnetometer measurements, *J. Geophys. Res.*, *116*, A07226, doi:10.1029/2010JA016226.

Turner, D. L., Y. Shprits, M. Hartinger, and V. Angelopoulos (2012), Explaining sudden losses of outer radiation belt electrons during geomagnetic storms, *Nat. Phys.*, *8*(3), 208–212, doi:10.1038/NPHYS2185.

Turner, D. L., S. K. Morley, Y. Miyoshi, B. Ni, and C.-L. Huang (2013), Outer radiation belt flux dropouts: Current understanding and unresolved questions, in *Dynamics of the Earth's Radiation Belts and Inner Magnetosphere*, edited by D. Summers et al., pp. 195–212, AGU, Washington, D. C., doi:10.1029/2012GM001310.

Ukhorskiy, A. Y., B. J. Anderson, P. C. Brandt, and N. A. Tsyganenko (2006a), Storm time evolution of the outer radiation belt: Transport and losses, *J. Geophys. Res.*, *111*, A11S03, doi:10.1029/2006JA011690.

Ukhorskiy, A. Y., B. J. Anderson, K. Takahashi, and N. A. Tsyganenko (2006b), Impact of ULF oscillations in solar wind dynamic pressure on the outer radiation belt electrons, *Geophys. Res. Lett.*, *33*, L06111, doi:10.1029/2005GL024380.

Vette, J. I. (1991), The AE-8 trapped electron model environment, *NSSDC/WDC-A-R and S 91-24*, NSSDC and WDC-A-R and S, Goddard Space Flight Center, Greenbelt, Md.

Walker, A. D. M. (1998), Excitation of magnetohydrodynamic cavities in the magnetosphere, *J. Atmos. Sol. Terr. Phys.*, *60*, 1279–1293.

West, H., J. Walton, and R. Buck (1972), Shadowing of electron azimuthal-drift motions near noon magnetopause, *Nat. Phys. Sci.*, *240*(97), 6–7.